Experimental and Numerical Study of a Turbulent Multiple Jets Issued from Lobed Diffusers

W. Medaouar [1], L. Loukarfi [1], M. Braikia [1], A. Khelil [1] and H. Naji [2, 3, †]

[1] Control, Testing, Measurement and Mechanical Simulation laboratory, University Hassiba Benbouali of Chlef, Hay Salem, National Road No. 19, 02000, Algeria
[2] University of Artois, Civil Engineering & Geo-Environment Laboratory (LGCgE- EA 4515), Technoparc Futura, F-62400 Béthune, France
[3] Northern Lille University France, LGCgE- EA 4515, FR-59000 Lille, France

† Corresponding Author Email: hassane.naji@univ-artois.fr

ABSTRACT

A combined experimental and computational study of a turbulent multiple jet from lobed diffusers is performed. The main interest of these multiple lobed jets is to come up with the best configuration that improves the thermal and dynamic homogenization in air diffusion units that can be used for ventilation, heating and air conditioning of residential premises. Herein, the configuration of a central lobed jet surrounded by six equidistant peripheral lobed jets has been investigated. On the experimental level, flow velocities and temperatures were measured by a multifunctional thermo-anemometer. In terms of numerical simulation, the conservation equations of mass, momentum and energy are solved while involving four turbulence models, viz., the k-ϵ model, the k-ω, the shear stress transport (SST) k-ω model and the Reynolds Stress Model (RSM). The findings are compared with thermo-anemometer measurements. It turns out that the SST k- ω model is most appropriate for predicting the average flow characteristics.

Keywords: Lobed jets; Multiple jets; Experimental study; Numerical simulation; Turbulence modelling; RANS.

NOMENCLATURE

a_1	turbulence modeling constant	W	lobed nozzle height
D	lobed nozzle inlet diameter	X,Y,Z	Cartesian coordinates
H	lobed nozzle length		
k	turbulent kinetic energy		
P_b	buoyancy production term	α, β, β^*	turbulence modeling constants
P_k	turbulent kinetic energy production		
$\mathbb{P}_k$	production limiter	μ, μ_τ	dynamic and turbulent viscosity, respectively
Re	Reynolds number		
S	spacing between the nozzles	ν, ν_ε	kinematic and effective viscosity, respectively
S_{ij}	mean strain rate tensor		
$\mathbb{S}$	invariant strain rate	ω	specific turbulent dissipation rate
T_0	jet temperature measured at the nozzles outlet	τ_{ij}	turbulent Reynolds stress tensor
T_i	jet temperature at different stations	θ_{in}	inner penetration angle
T_{in}	jet temperature at the inlet of the nozzle	θ_{out}	outer penetration angle
T_a	ambient temperature		
U_0	average jet velocity measured at the exit of the nozzle	Subscripts/Superscripts	
		0	exit
U_i	jet velocity at different stations	a	ambient
U_{in}	average velocity at the inlet of the nozzle	in	inlet
U_r	reduced velocity	out	outlet
		r	reduced

1. INTRODUCTION

Improve the process of mixing turbulent flows to obtain beneficial results such as the combustion efficiency and pollutants emission reduction, for example, is of great interest. This mixing process governs ventilation systems, which play a major role in meeting the needs for residential premises occupants in terms of thermal comfort while dropping energy consumption. A better mix of jet with the ambient air will satisfy occupants in terms of thermal comfort and air quality. One of improving flows mixing methods is to use multiple jets. A multiple-jet configuration includes two or more jets discharged from the same exit plane, separated by a finite distance. The jets interact with each other after a short distance from the exit plane. Multiple jets are widely used today in the industry. They are found in applications such as drying paper, textiles, ceramics, cooling electronic components, ventilation and air conditioning of premises, among other applications.

Passive techniques to control jet flow consists of blowing the jet through asymmetrical nozzles, e.g., tabbed nozzles, chevron, nozzles, lobed nozzles, to name a few. A lobed nozzle has a circular cross-section at the inlet and a curled shape at the exit. It generates strong streamwise structures at the outlet of the nozzle itself, which improves mixing in the jet near field.

Basically, literature studies can be split up into two categories: experimental and numerical studies. Several experimental studies have been carried out to the improvement of the thermal comfort in the premises. The study of Meslem *et al.* (2008) allowed a quantification of the induction gain of two lobed jets compared to a reference circular jet with the same flow rate and the same blowing section. The authors used three nozzles: a circular nozzle as a reference and two lobed nozzles, the first being a straight lobed nozzle without inclination, while the second is a lobed nozzle with a double inclination. They noted that, if the induction gain of the jet from the first nozzle scarcely exceeds 70% with respect to the reference circular jet, the jet induction gain from the second nozzle reaches up to four times that of the circular jet.

To better understand the influence of vortex dynamics on induction, Nastase and Meslem (2008) experimentally explored the initial region of a round jet and a lobed jet from a lobed orifice. The authors concluded that in both cases induction is provided by longitudinal structures. They stated that, in the circular jet, the induction is modulated at the Kelvin-Helmholtz ring structures passage frequency, whereas for the lobed jet, the effect of the Kelvin-Helmholtz structures is neutralized.

Meslem *et al.* (2010) experimentally investigated twin cross-jets in comparison with twin circular jets for the same initial Reynolds number and spacing. These authors concluded that: 1) mixing between cross-lobed jets is more efficient and mixing point occurs earlier, 2) the driven flow rate caused by the lobed orifices reaches 3 times the value of the circular twin jet, 3) a row of cross jets generates a more uniform overall flow than in the case of the circular jets, 4) in both cases (twin jets and row jets), the cross orifice generates a flow having a longer throw, and 5) the air flow induced in the case of the lobed perforated panel is on average twice as high as that of the circular perforated panel.

The draft risk (DR) index was used by Nastase *et al.* (2011) to quantify the impact of a rectangular air diffusion grille with lobed fins on local thermal comfort. This grille allowed to achieve better DR values in the occupied zone compared to those with a straight wing grille.

Braikia *et al.* (2012) implemented a study in which they explored different multiple swirling jet configurations. The authors emphasized the improvement of the thermal homogenization of the dealt area with an appropriate choice of air blowing position. It appears that the central jet plays a significant role in improving thermal homogenization. To sum up, the authors concluded that: 1) for the double swirling jet, the spacing between the blow orifices reduces the temperature radial amplitude, while ensuring both a substantial spreading and homogenization. From a dynamic point of view, the spacing between orifices causes a decrease in the blowing velocities and delays the jets fusion while increasing the fluctuation intensities, 2) the temperature decreases less rapidly for the configuration with three and four swirling jets in a triangle arrangement, when all jets are all active, compared to the single swirling jet. Indeed, the central jet modifies the adjacent behavior of the peripheral jets, improves the flow homogenization and induces a monotonous temperature decrease, and 3) in the far field, the configuration with seven swirling jets leads to an almost perfect homogenization.

Bennia *et al.* (2016) compared the dynamic profiles at the main plane of a lobed nozzle with those at the secondary plane in order to test its performance in terms of ambiances homogenization. The authors found that dynamics profiles are more spread at the main plane in the potential core region compared because of the lobes wider opening. However, far from the central core, the dynamic profiles are similar to those of a circular jet indicating that the lobe shape had no influence.

Bragança *et al.* (2016) considered a ceiling-mounted three-cone diffuser operating in heating mode and equipped with lobes to experimentally analyze the thermal comfort, the jets characteristics and the air flow profile. Their analysis led to an improvement of the thermal comfort without pressure loss increase and without additional energy consumption compared to a conventional diffuser.

Numerically, the multiple jets topic has been dealt through several studies where the most studied parameters are the nozzles spacing, the geometry and the diameter of the nozzles, the number of jets and their arrangements.

For this aim, Anderson and Spall (2001) assessed the performance of turbulent RSM model and the standard k-ε model to simulate two turbulent

rectangular parallel jets. Numerical predictions were compared to the experimental results using hot wire anemometer. The comparison revealed an excellent agreement on the merge location and combined point. In addition, the considered CFD methods were able to predict mean velocity profiles in the symmetry plane with good precision. The amplitude and decay of predicted normal stress profiles along the symmetry plane of the flow field corroborate the experimental results. However, the two turbulence models showed a narrower width of the jet envelope than that measured experimentally.

Meslem *et al.* (2011) have numerically studied a turbulent flow of a cross-shaped turbulent double jet using the standard *k-ε* model, the shear stress transport (*SST*) *k-ω* model and the Reynolds stress model (*RSM*) and compared their results to PIV measurements. They showed that the k-ε and RSM models are more suitable for predicting the length of the potential jet core, the variation of the centerline velocity and the flow spreading in the symmetry plane of the twin jet. However, these models have been found to overestimate overall flow expansion and jet flow. As for the *SST k-ω* model, it seems more appropriate to predict turbulent average quantities, jet interaction, overall expansion, and ambient air induction when the flow is numerically resolved through a lobed diffuser. It dawns from their study that none of the three turbulence models properly predicts all flow characteristics. Despite these lacks, these authors advise the use of the *SST* model *k-ω* to help designing HVAC applications.

Depuru Mohan *et al.* (2015) numerically compared the mixing performance of a single lobed jet to two configurations of multiple jets (circular and lobed) for the same flow rate at the nozzles inlet using the standard k-ε turbulence model. They considered the temperature a passive scalar to typify the mixture. In addition, they stated that: a) the jet core length is shortest in multiple lobed thereby indicating its superior mixing capability, and b) the entrainment velocity is highest in multiple lobed jet, which draws more ambient air into the jet, thus achieving mixing effectively. They concluded that it is better to have several jets instead of a single jet having the same momentum flux at the nozzle exit.

Khelil *et al.* (2016) have numerically examined the interaction between several swirling jets mounted in unbalanced positions by handling turbulence using the *k-ε, RNG k-ε* and *RSM* turbulence models. From the numerical investigation performed, the authors showed that the RSM model was better suited than the standard k-ε model for capturing the mean flow behavior. Through the flow characteristics analysis, they demonstrated that the mixing between the swirling jets generated a temperature distribution along the centerline and near the blowing diffusers, while allowing the resulting jet to propagate.

Kannan and Panchapakesan (2017) numerically studied multiple circular jets (from one to five) flowing into a calm air environment using Open FOAM computation code. They compared their findings to the available experimental data and found that it is the standard k-ε turbulence model that satisfactorily reproduces the non-linear decay of the mean axial velocity for the multiple jets case. They have successfully exhibited entrainment, secondary flows, and average turbulent kinetic energy within the multiple jets.

This paper organization is as follows: Section 2 deals with a brief description of the experimental setup and techniques. Section 3 provides working conditions while briefly depicting multiple lobed jets' configuration. Section 4 presents and comments experimental data. Section 5 is designated to the mathematical modeling adopted and the computational procedure while supplementing them with the boundary conditions (BCs), generation and independence of the mesh. Section 6 devotes the obtained findings and their comparison with experimental data. Finally, conclusions from the present study are drawn in Section 7.

2. EXPERIMENTAL SETUP AND TECHNIQUES

The experiments were carried out in a room measuring $3.5\text{x}3.8\text{x}2.9$ m^3 (LxWxH). The experimental installation consists of a metal frame on which is fixed a plexiglass plate. On the latter, seven devices with lobed diffusers blowing hot air are put and directed downwards (Fig. 1). The temperatures (T_i) and the velocities (U_i) of the jet are measured by a multifunctional thermo-anemometer (Velocicalc Plus type). The data are displayed on a screen in a spreadsheet before being transferred to a computer for statistical processing. Temperatures and velocity of the flow are measured by a hot wire anemometer (type Velocicalc Plus Air velocity Meter), which is a high-precision multifunctional instrument. The data can be viewed on a screen, printed or downloaded to a spreadsheet program allowing us to easily transfer data to a computer for statistical treatment. The accuracy is of order $\pm 0.015\,m/s$ for velocity and $\pm 0.3°C$ for temperature from thermal sensor. The thermal sensor is supported by rods that are easily guided vertically and horizontally to scan a maximum space in all three directions. In addition, a digital thermometer was placed (outside the jet) to instantly measure ambient temperature (T_a).
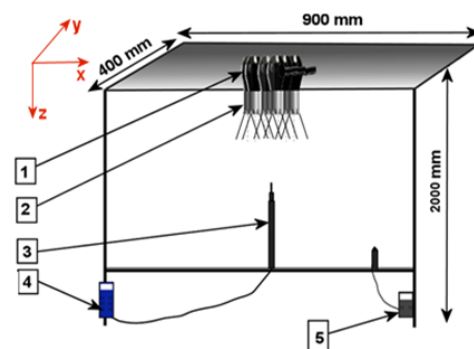
1- Hair dryer; 2- Lobed nozzles; 3- Thermo-anemometer probe; 4- Thermo-anemometer; 5- Thermometre

Fig. 1. Schematic diagram of experimental setup.

3. WORKING CONDITIONS

Figure 2 shows the geometry of the lobed diffusers used in this study. The nozzle consists of a circular tube of diameter D = 40 mm with a daisy shape at the exit. The exit plane has six inclined lobes with parallel sides and six sinusoidal troughs. The inner and outer penetration angles are θ_{in} = 22° and θ_{out} = 14°, respectively. The length (H) and height (W) of each lobe is 15 mm and 6 mm, respectively.

The configuration studied (Fig. 3) is a 7 lobed jets comprising a central jet surrounded by 6 equidistant peripheral jets. It should be noted that this configuration was chosen because it proved to be the most efficient in terms of thermal homogenization and non-stratification for multiple swirling jets (Braikia *et al.,* 2012). The spacing ratio between nozzles is S/D = 2.5. The reference velocity U_0 and the temperature T_0 measured at the outlet of the jets are respectively 9.20 m/s and 63 °C. The jet Reynolds number (Re = $U_{in}.D/\nu$) is 1.8443x10^4.
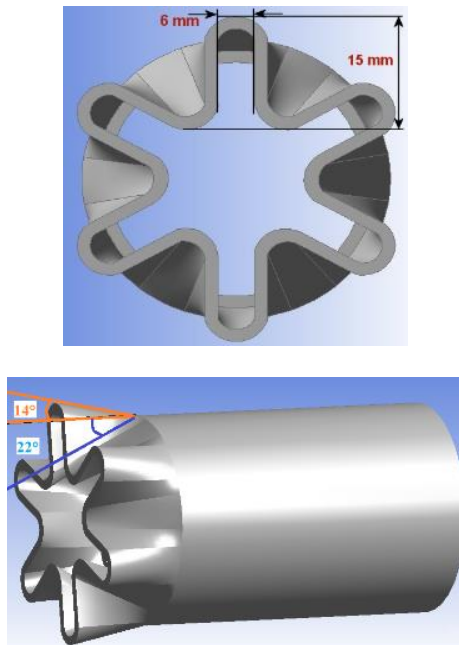
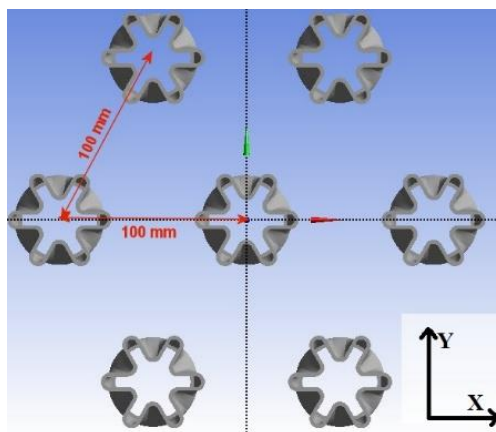**Fig. 2. Geometry of lobed diffusers.**

Fig. 3. Multiple lobed jet configuration.

4. RESULTS AND DISCUSSION

4.1 Velocity and temperature measurements (axial distribution)

Figure 4 shows the axial distribution of the reduced velocity $U_r = U_i/U_0$ $U_r = U_i/U_0$ and the reduced temperature $T_r = (T_i - T_a)/(T_0 - T_a)$ over an axial distance of 20 jet diameters from nozzles outlet. It can be seen that the velocity and temperature profiles can be split into 3 regions: a first which extends to 1 jet diameter at the nozzles outlet where the velocity and temperature remain equal to their reference values U_0 and T_0. In this region, jets behave as a single jet, indicating that the interaction between the jets has not yet started. Moving away a little further from the axial station Z/D = 2, a second region appears where the axial velocity decreases rapidly. The temperature will also undergo a rapid decrease up to 10 jet diameters. This decrease can be explained by the energy transfer towards the radial direction due to jets interaction. Beyond the axial station Z/D = 10, a third region appears with weak gradients between the values indicate that the velocity and temperature tend to stabilize (curves less accentuated).
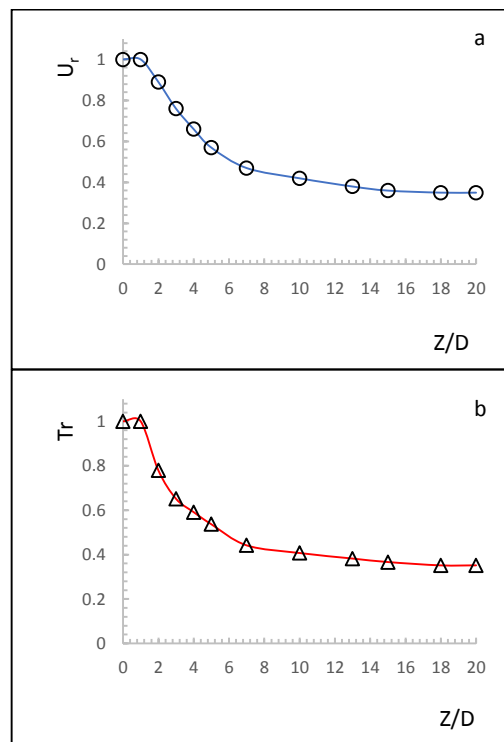

Fig. 4. Axial distribution of a) measured velocity and b) temperature profiles of multi-lobed jet.

4.2 Velocity Measurements in X- and Y-Directions

Figures 5 and 6 show the measured velocity profiles along X- and Y-directions for different axial locations selected (Z/D = 1, 3, 5, 7, 10, 20), respectively. According to the X-direction (Fig. 5), fairly sharp maxima and minima take place near blowing surface (Z/D ≤ 5) indicating that the maximum and minimum velocities are close to the
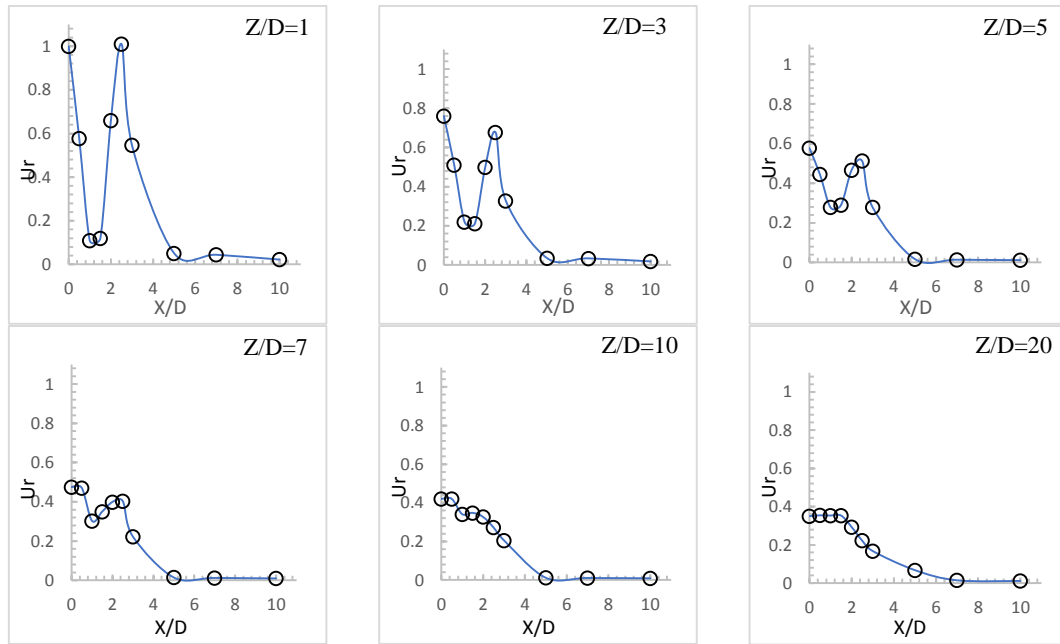
Fig. 5. Velocity measurements of the multiple lobed jet in X-direction.
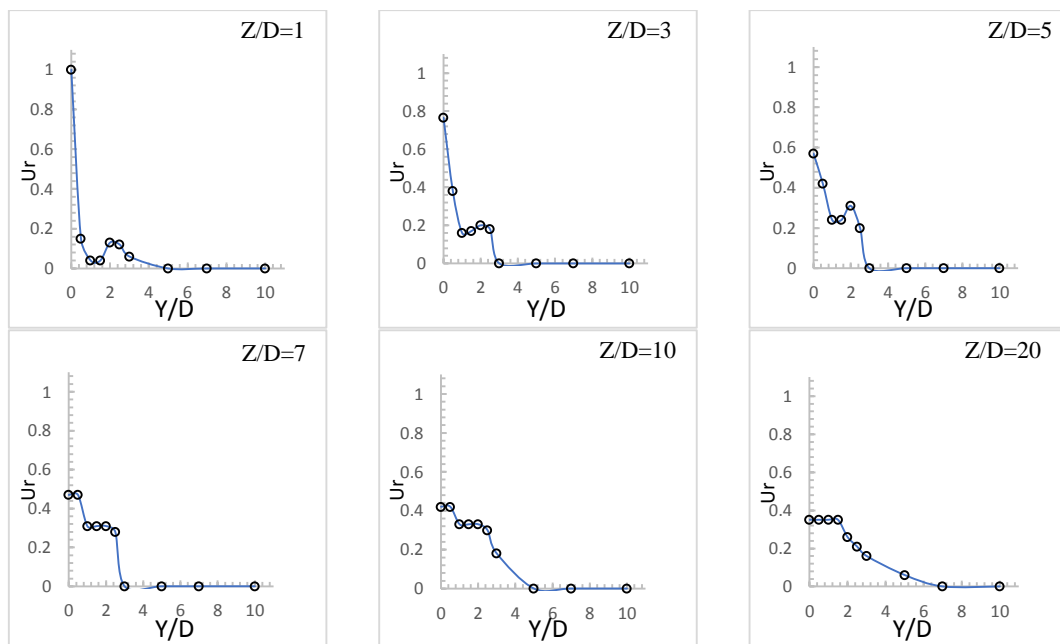
Fig. 6. Velocity measurements of the multiple lobed jet in Y-direction.

diffusers exit. Near the exit of the diffusers (small axial stations, $Z/D \leq 5$), a recirculation zone comes about while inducing the minimum velocity. From the axial station $Z/D = 2$ (not shown here), jets begin to interact with each other and the decrease of the maximum values is offset by an increase of minimum values. Beyond $Z/D = 10$, the velocity profiles begin to stabilize to exhibit curves similar to those of a single jet. In the Y-direction, it can be seen that the velocity values are less spread in the near field because of the asymmetry of the studied configuration. These profiles start to

propagate as we move away from the jets exit plane in the axial direction.

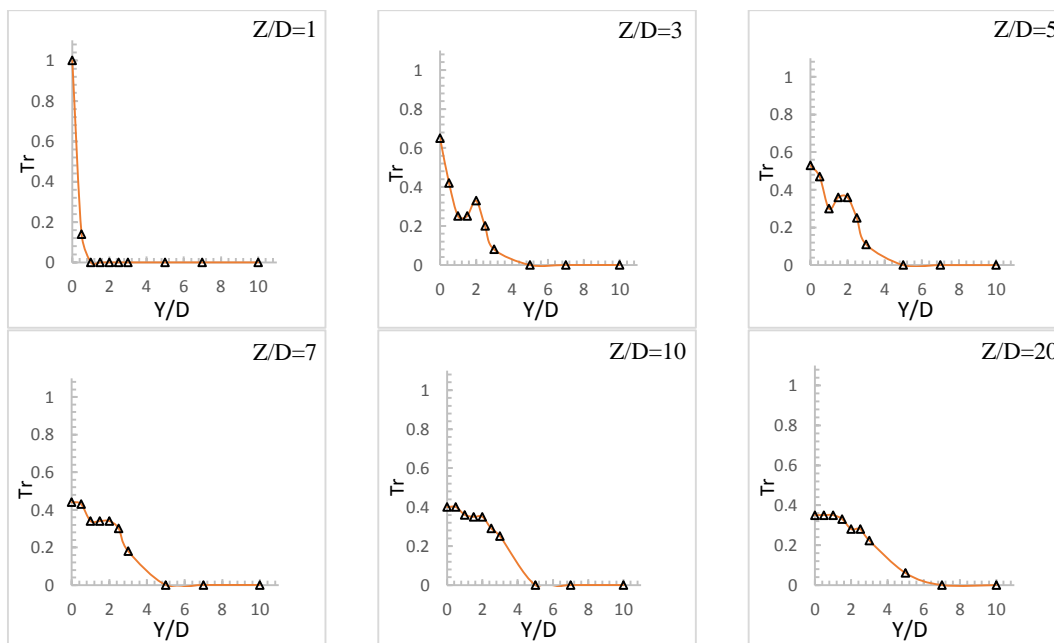### 4.3 Temperature Measurements in X- and Y-Directions

Figures 7 and 8 provide the measured temperature profiles along X- and Y-directions for different axial locations selected ($Z/D = 1, 3, 5, 7, 10, 20$), respectively.

In the X-direction, it can be seen that the maximum temperature is reached very close to blowing orifices ($Z/D = 1$) with noteworthy amplitudes at the station
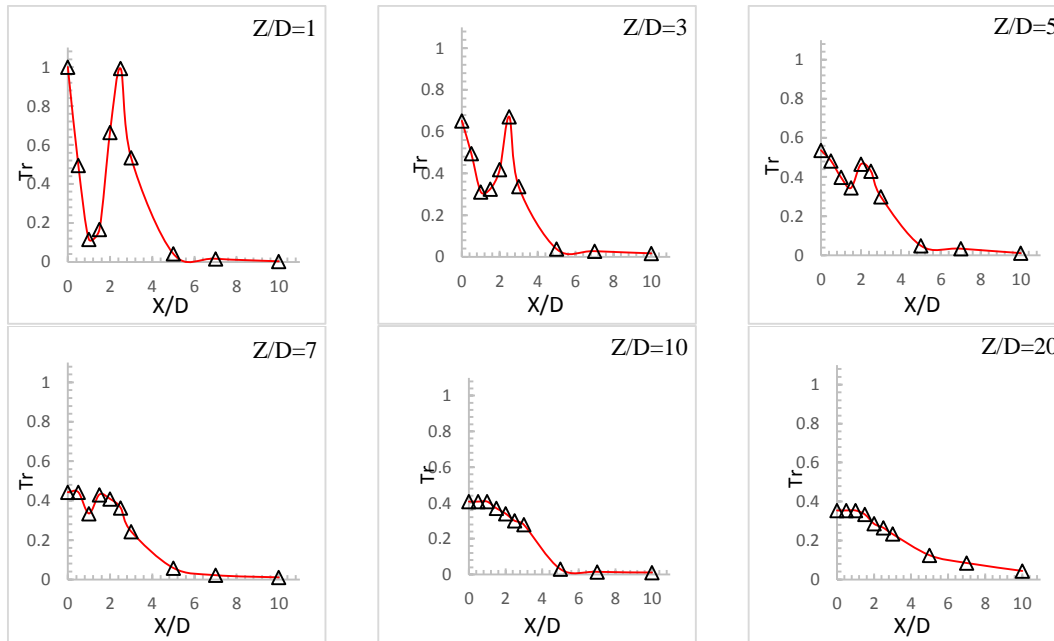
Fig. 7. Temperature measurements of the multiple lobed jet in X-direction.

Fig. 8. Temperature measurements of the multiple lobed jet in Y-direction.

X/D=1 and X/D = 3. At this distance, the jets have not yet interacted with each other. Towards the axial direction and from Z/D > 3, these amplitudes start to decrease from one station to another and curves irregularities gradually disappear, which indicate a thermal stability initiation.

Beyond Z/D = 10, the temperature profiles tend to flatten out showing a flow thermal homogenization. At approximately 20 times the diameter of a jet, in the axial direction of the flow, the resulting jet temperature approaches the part ambient temperature. In the near field of the multiple jet (Z/D < 10), in the Y-direction of the flow, the temperature profiles are different from those in the X-direction due to the asymmetric arrangement of the nozzles. Beyond Z/D = 10, these profiles become similar.

Figure 9 depicts a comparison of the velocity and temperature profiles in the X- and Y-directions at two axial stations (Z/D = 3 and Z/D = 10). Note that from Z/D = 10, these profiles become similar meaning that their asymmetry has disappeared and that the resulting jet goes to be axisymmetric.
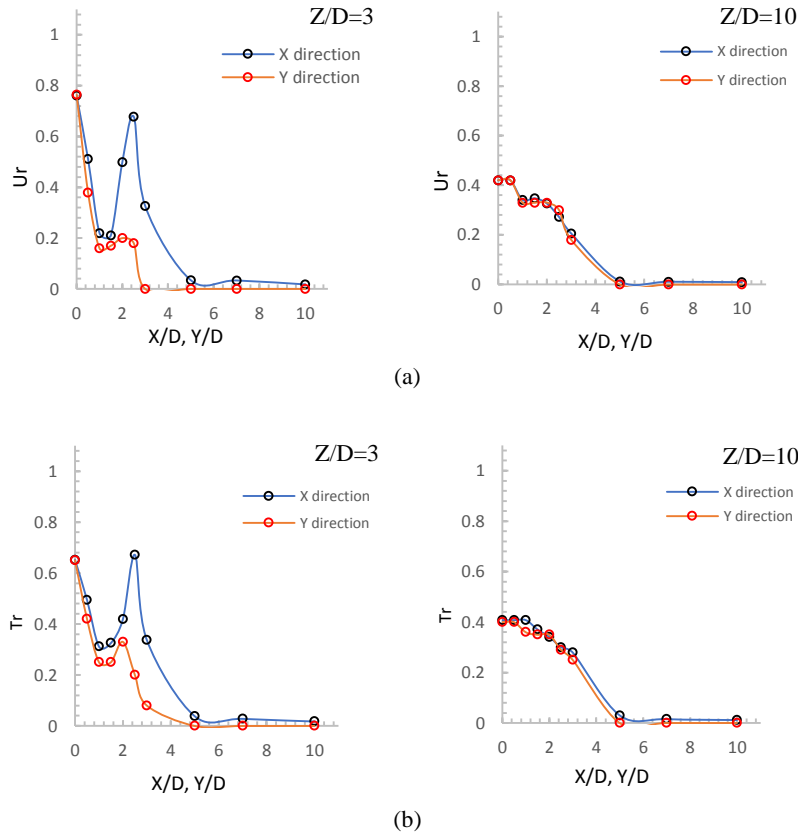
734

(a)

(b)

Fig. 9. (a) Velocity and (b) temperature profiles in X- and Y-direction at Z/D=3 and Z/D=10.

5. COMPUTATIONAL SETUP

5.1 Mathematical Modeling

In this study, the incompressible flow is assumed to be steady, three-dimensional and turbulent. Note that here air is the working fluid, and turbulent Reynolds stresses ($\tau_{ij} = \rho \overline{u_i' u_j'}$) are computed as usual in two-equation models via the Boussinesq expression. In this framework, the governing equations of conservation of mass, momentum and energy are written in tensor notation in Cartesian coordinates as follows:

$$\frac{\partial}{\partial x_i}(U_i) = 0 \tag{1}$$

$$\frac{\partial}{\partial x_j}(U_i U_j) = -\frac{\partial p}{\partial x_i} + \frac{\partial}{\partial x_j}\left[\nu\left(\frac{\partial U_i}{\partial x_j} + \frac{\partial U_j}{\partial x_i}\right) - \overline{u_i' u_j'}\right] \tag{2}$$

$$U_i \frac{\partial T}{\partial x_i} = \frac{\partial}{\partial x_i}\left[\frac{\lambda}{\rho C_p}\frac{\partial T}{\partial x_i} - \overline{u_i' T'}\right] \tag{3}$$

where *U, p* and *T* denote average velocity, pressure and temperature, respectively. μ is the dynamic viscosity, C_p is the thermal capacity, and λ is the thermal conductivity. The resolution of these equations requires a turbulent closure model capable of properly characterizing the fluctuating quantities, viz., mean Reynolds stresses τ_{ij} and the turbulent heat flux ($\rho C_p \overline{u_i' \hat{T}}$). As mentioned up, four turbulence models were considered for assessment. These are the standard k-ϵ (*Ske*) model, the standard k-ω (*Sko*, the *SST* k-ω model and the RSM model. Here, we just mention them briefly.

$$-\rho \overline{u_i' u_j'} = \mu_t \, 2S_{ij} - \frac{2}{3}\rho k \, \delta_{ij} \tag{4}$$

where μ_t an eddy viscosity, S_{ij} is the mean strain rate tensor, and k is turbulent kinetic energy. Turbulent viscosity μ_t depends on the turbulent kinetic energy *k* and its dissipation rate ε predicted, according to the relationship (5)

$$\mu_t = \rho C_\mu k^2 / \varepsilon \tag{5}$$

The following Eqs. (6) and (7) represent the turbulent eddies influence, and they are added to the averaged Navier–Stokes equations to obtain an average map of the turbulence distribution, considering $\nu_e = \nu + \nu_t / \sigma$:

$$\frac{\partial}{\partial x_i}(k u_i)$$
$$= \frac{\partial}{\partial x_j}\left[\nu_e \frac{\partial k}{\partial x_j}\right] + P_k + P_b - \epsilon \tag{6}$$

$$\frac{\partial}{\partial x_i}(\epsilon u_i)$$

$$= \frac{\partial}{\partial x_j}\left[\nu_e \frac{\partial \epsilon}{\partial x_j}\right] + C_{1\epsilon}\frac{\epsilon}{k}P_k + C_{1\epsilon}(1-C_{3\epsilon})\frac{\epsilon}{k}P_b$$

$$-C_{2\epsilon}\frac{\epsilon^2}{k}$$

(7)

In Eqs. (6)-(7), P_k and P_b represents, respectively, the turbulent kinetic energy production and the buoyancy production term whose expressions are:

$$P_k = 2\nu_t S_{ij}\frac{\partial U_j}{\partial x_i}; \quad P_b = -g_i \frac{\nu_t}{\sigma_T \rho}\frac{\partial \rho}{\partial x_i} \ .$$

σ_T being the ratio of the turbulent to thermal eddy viscosities whose value 0.85 has been considered herein.

The values of the model constants in *Ske* model are:

$$C_{1\epsilon} = 1.44 \ , \ C_{2\epsilon} = 1.92, \ C_\mu = 0.09 \ , \sigma_k = 1.0 \ , \sigma_\epsilon = 1.3 \ , \ \sigma_T = 0.85$$

• RSM

The RSM model (Chou, 1945; Rotta, 1951) does not consider Boussinesq assumption. Therefore, it directly resolves all six components of the Reynolds stress tensor using their modeled transport equations while taking into account the turbulence's history and anisotropy. These findings suggest that the RSM model better simulates turbulence effects than RANS turbulence models based on turbulent viscosity assumption. Nevertheless, RSM requires a variety of empirical data that limits its applications.

The RSM that has been considered here can be summarized as follows:

$$\underbrace{\frac{\partial}{\partial x_k}\left(\rho U_k \overline{u_i' u_j'}\right)}_{C_{ij} \equiv Convection} = \underbrace{+\frac{\partial}{\partial x_k}\left[\mu \frac{\partial}{\partial x_k}\left(\overline{u_i' u_j'}\right)\right]}_{D_{L,ij} \equiv Molecular\ Diffusion}$$

$$\underbrace{-\frac{\partial}{\partial x_k}\left[\rho\ \overline{u_i' u_j' u_k'} + p\left(\delta_{kj}u_i' + \delta_{ik}u_j'\right)\right]}_{D_{T,ij} \equiv Turbulent\ Diffusion}$$

$$\underbrace{-\rho\left[\overline{u_i' u_k'}\frac{\partial U_j}{\partial x_k} + \overline{u_j' u_k'}\frac{\partial U_i}{\partial x_k}\right]}_{P_{ij} \equiv Stress\ Production} - \underbrace{2\mu\ \overline{\frac{\partial u_i'}{\partial x_k}\frac{\partial u_j'}{\partial x_k}}}_{\varepsilon_{ij} \equiv Dissipation}$$

$$+ \underbrace{p\left(\frac{\partial u_i'}{\partial x_j} + \frac{\partial u_j'}{\partial x_i}\right)}_{\phi_{ij} \equiv Pressure\ Strain}$$

$$- \underbrace{\rho\beta\left(g_i\overline{u_j'\theta} + g_j\overline{u_i'\theta}\right)}_{P_{b,ij} \equiv Buoyancy\ Production}$$

(8)

Of the various terms in these exact equations, C_{ij}, $D_{L,ij}$, and P_{ij} do not require any modeling. However, $D_{T,ij}$, ε_{ij}, ϕ_{ij}, and $P_{b,ij}$, , and need to be modeled to close these equations. Other forms of terms, in their order of appearance, may be used as shown below (Lien and Leschziner, 1994):

$$C_{ij} = D_{L,ij} + D_{T,ij} + P_{ij} + \varepsilon_{ij} + \phi_{ij} + P_{b,ij}$$

(9)

with:

$$D_{T,ij} = \frac{\partial}{\partial x_k}\left[\frac{\mu_t}{\sigma_k}\frac{\partial}{\partial x_k}\left(\overline{u_i' u_j'}\right)\right] . \ \varepsilon_{ij} = -2\rho\varepsilon\delta_{ij}\ /3$$

$$\phi_{ij} = -C_1\rho\frac{\epsilon}{k}\left(\overline{u_i' u_j'} - \frac{2k\delta_{ij}}{3}\right) - C_2\left(P_{ij} - \frac{2}{3}P\delta_{ij}\right)$$

$$P_{b,ij} = -3C_\mu k\ /\left(2\sigma_T\ \varepsilon\right)\left(\overline{u_j' u_k'}\frac{\partial\overline{\rho}}{\partial x_k}\right)g_i$$

The transport equation for the Reynolds stress tensor is supplemented by that of the dissipation rate (7) (*see BC-Ske model*).

Standard empirical constants were used:

$$C_1 = 1.8; \ C_2 = 0.6; \ C\varepsilon_1 = 1.45; \ C\varepsilon_2 = 1.$$

• Standard k-ω (Sko)

The standard k-ω model considers the low Reynolds number effect, which can be calculated directly up the wall. Thereby, such a model could provide reasonable results for simulating near-wall flow compared to the standard k-ε model. Nevertheless, it remains an isotropic turbulence model. The governing equations of Wilcox's original k-ω model for steady-state turbulent flow are as follows (Wilcox, 1998):

$$U_j\frac{\partial k}{\partial x_j} = \frac{\partial}{\partial x_j}\left[(\nu + \sigma_k\nu_t)\frac{\partial k}{\partial x_j}\right] + P_k - \beta^* k\omega$$

(10)

$$U_j\frac{\partial\omega}{\partial x_j} = \frac{\partial}{\partial x_j}\left[(\nu + \sigma_\omega\nu_t)\frac{\partial\omega}{\partial x_j}\right] + \alpha\frac{\omega}{k}P_k - \beta\omega^2$$

(11)

$$\nu_t = \frac{k}{\omega}$$

(12)

ω being e specific dissipation rate.

where $\alpha = 5/9; \ \beta = 3/40; \ \beta^* = 0.09; \ \sigma_k = 0.5 = \sigma_\omega$.

• SST k-ω (SST-ko)

Menter's k-ω shear stress transport (SST) model comprises two equations (Wilcox, 1998; Versteeg and Malalasekera, 2007; Menter, 1994; Menter and Egorov, 2010):

• one for k, the turbulent kinetic energy (Eq. (12)):

$$U_j\frac{\partial k}{\partial x_j} = \frac{\partial}{\partial x_j}\left[(\nu + \sigma_k\nu_t)\frac{\partial k}{\partial x_j}\right] + \mathbb{P}_k - \beta^* k\omega$$

(12)

• and one for ω, the specific turbulent dissipation rate (13):

$$U_j\frac{\partial\omega}{\partial x_j} = \frac{\partial}{\partial x_j}\left[(\nu + \sigma_{\omega 1}\nu_t)\frac{\partial\omega}{\partial x_j}\right] + \alpha\mathbb{P}_k - \beta\omega^2 + 2(1 - F_1)\frac{\sigma_{\omega 2}}{\omega}\frac{\partial k}{\partial x_i}\frac{\partial\omega}{\partial x_i}$$

(13)

where the eddy viscosity ν_t is given by:

$$\nu_t = a_1 k \,/\, \max\left(a_1\omega, SF_2\right) \tag{14}$$

given that **S** $(=2S_{ij}S_{ij})^{1/2}$ is the strain rate invariant measure, a_1 $(= 0.31)$ is a constant, ν_t is the kinematic eddy viscosity and F_2 is a blending function (Costa Rocha *et al.*, 2016) given by the Eq. (15):

$$F_2 = \tanh\left[\left[max\left(\frac{2\sqrt{k}}{\beta^*\omega y}, \frac{500\nu}{y^2\omega}\right)\right]\right] \tag{15}$$

$\mathbb{P}_k$ is a production limiter to prevent turbulence build-up in stagnation regions (Menter *et al.*, 2003), and is given by the following relationship:

$$\mathbb{P}_k = min(P_k, 10\beta^*\omega) \tag{16}$$

$P_k = 2\nu_t S_{ij}\frac{\partial U_i}{\partial x_j}$ being the turbulent kinetic energy production.

The other blending function F_1 is defined as follows (Costa Rocha *et al.*, 2016):

$$F_1 = \tanh\left\{\left\{min\left[max\left(\frac{\sqrt{k}}{\beta^*\omega y}, \frac{500\nu}{y^2\omega}\right), \frac{4\sigma_{\omega2}k}{D_\omega y^2}\right]\right\}\right\} \tag{17}$$

with $D_\omega = max\left(2\dfrac{\sigma_{\omega2}}{\omega}\dfrac{\partial k}{\partial x_i}\dfrac{\partial\omega}{\partial x_i}, 10^{-10}\right)$.

Each model coefficient $\emptyset$ $(= \sigma_k, \sigma\omega, \alpha$ and β can be evaluated from the following relationship:

$$\phi = F_1\phi_1 + (1 - F_1)\phi_2 \tag{18}$$

where indices 1 and 2 are connected to the adjusted k-ω model and the *Ske* model, respectively. Thereby, the constants' values of the SST k-ω closure model can be summarized as follows:

$$\alpha_1 = 5\,/\,9 \qquad \alpha_2 = 0.44 \qquad \beta_1 = 3\,/\,40$$

$$\beta_2 = 0.0828 \qquad \beta^* = 0.09 \qquad \sigma_{k1} = 0.85$$

$$\sigma_{k2} = 1 \qquad \sigma_{\omega1} = 0.5 \qquad \sigma_{\omega2} = 0.856$$

5.2 Solution Procedure

The computational fluid dynamics code used for turbulence simulation is ANSYS FLUENT 18.1 solver based on the finite volume method. An implicit pressure-based solver is adopted. The SIMPLE algorithm is used for pressure-velocity coupling.

5.3 Boundary Conditions (BC)

The boundary conditions used in this study are depicted in Fig. 10. In the context of the models adopted here, these conditions are: A velocity and a temperature at the inlet of 6.7 m/s and 65 ° C, a turbulence intensity (I_{in}=4 %), a Reynolds number ($Re = 1.8443\text{x}10^4$), the air density and its dynamic viscosity being equal to 1.225 kg/m^3 and 1.78x10^{-5} kg/m.s, respectively. The solution is considered converged when residuals are below 10^{-6} for the temperature and 10^{-5} for the other quantities.

5.4 Mesh generation

Meshing of the nozzles and the domain have been achieved via ANSYS ICEM CFD 18.1 with unstructured tetrahedral cells. It is non-uniform with high density in areas high interest compared to other areas with a grid refinement towards the lobes and through the nozzles (Fig. 11).
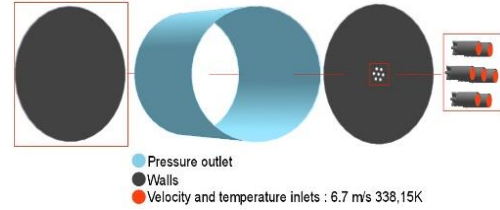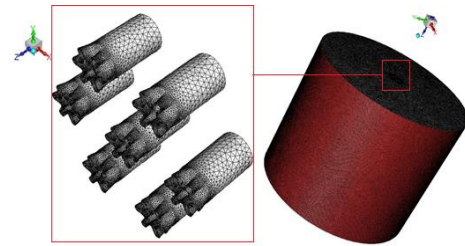

Fig. 10. Boundary conditions.

Fig. 11. Mesh of the computation domain.

5.5 Mesh Independence

Five grids are used to analyze the impact of grid resolution on the simulation results ranging from a coarse grid with 598,674 cells to a more refined grid with 6,704,011 cells (Table 3). Figure 12 shows the different adaptations of the mesh so that the solution is independent of the mesh.

Table 1 Different mesh sizes used

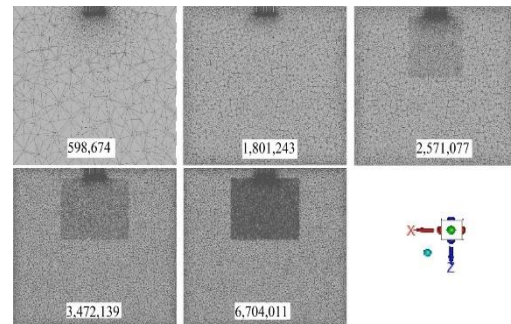| Grid 1	598,674 cells
Grid 2	1,801,243 cells
Grid 3	2,571,077 cells
Grid 4	3,472,139 cells
Grid 5	6,704,011 cells

Fig. 12. Refinements of the different meshes considered.

For the results to be considered reliable, grid convergence analysis is required to disassemble the accuracy of a CFD code. Figure 13 illustrates the axial distribution of the dimensionless U_r profiles for the five coarse grids via the *SST k-ω* model. It is observed that the difference between coarse and refined grids is trivial. As a result, it turns out that the

use of the grid 5 with 3,472,139 cells is appropriate in this study, since the maximum error between the grids 4 and 5 is 2% (i.e., insignificant). Therefore, grid 4 was considered to perform all the simulations presented hereinafter.
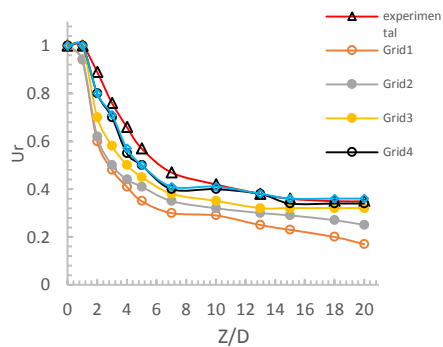
Fig. 13. Grid influence on dimensionless velocity U_r obtained from the *SST k-ω* model.

## 6 RESULTS AND DISCUSSIONVelocity and Temperature (Axial Distribution)

In this section, the validation, the simulation results with the different turbulence models are presented. Figure 14 presents the axial evolution of U_r and temperature with the four numerical models *Ske*, *Sk-ω*, *SST k-ω* and RSM compared with experimental results. All profiles are almost comparable to each other. However, it is the *SST k-ω* model that better corroborates the experimental results. Far from the blowing plane, the *Sk-ω, SST k-ω* models slightly underestimate speed profiles and overestimate temperature profiles, while *Ske* and *RSM* models fail to predict the axial velocity decay and the temperature in the far field. In other words, the results from the *SST k-ω* model compare favorably with the experimental data with a maximum difference of 11% for velocity and 7% for temperature. This suggests that it correctly handles the interaction between lobed jets. Thereby, we chose it to pursue the numerical study.

6.2 Velocity and Temperature (X- and Y-Directions)

The numerical simulation results presented in Figs. 15 and 16 concern the U_r-velocity evolution along the X- and Y-directions at different axial stations provided by the *SST k-ω* model. It can be noted that the *SST k-ω* entirely predicts the velocity distribution coinciding well with the experimental measurements.

To further assess the SST k-ω model against the experimental data, eight locations (Z/D =1, 3, 7, 10, 15, 20) were selected for the temperature comparison. The temperature plots are illustrated in Figs. 17 and 18. Again, a thorough review of this figure shows that numerical predictions better corroborate experimental data along axes, regardless of the axial position, confirming thereby that the model is suitable for simulating jets issued

from lobed diffusers.
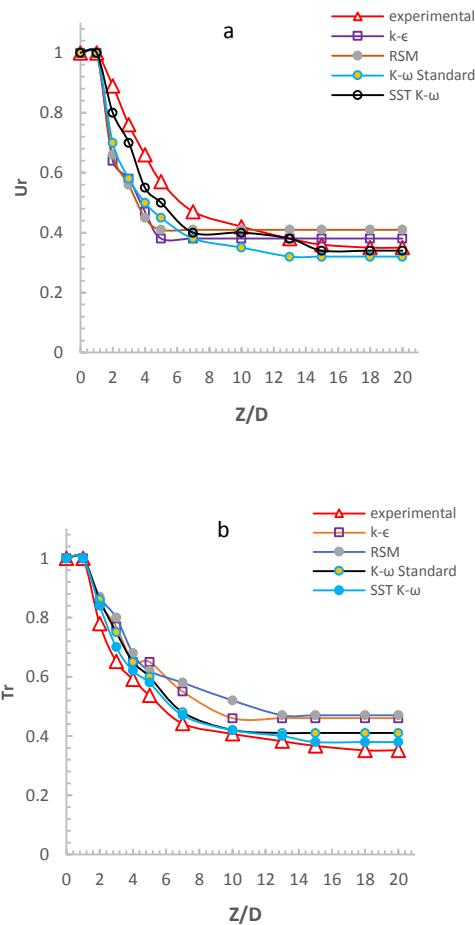
Fig. 14. Comparison of axial velocity (a) and temperature (b) profiles from *Ske, Sk-ω, SST k-ω* and RSM models with experimental results.

6.3 Temperature Contours

Figure 19 depicts average temperature contours coming from the *SST k- ω* model at different axial stations (Z/D = 1, 2, 3, 4, 5, 10, 15, 20). Three zones appear that have been exhibited via the experimental results. The first zone extends over a diameter of jets' outlet, where the peripheral jets begin to mix with the ambient air while attracting towards the central jet but without any interaction between the jets themselves. In the second zone between stations Z/D = 2 and Z/D = 10, the jets interact and merge while ensuring a diffusion of the resulting jet. Beyond the station Z/D = 10, there is the third zone where the temperature profiles are uniform to gather to a single circular jet profile towards the station Z/D = 20 where the resulting jet temperature approaches the ambient temperature.

7. CONCLUSION

This study deals with experimental and numerical study of a turbulent multiple jets from lobed diffusers. Four turbulence models have been initially selected to finally retain only the SST *k-ω* model.
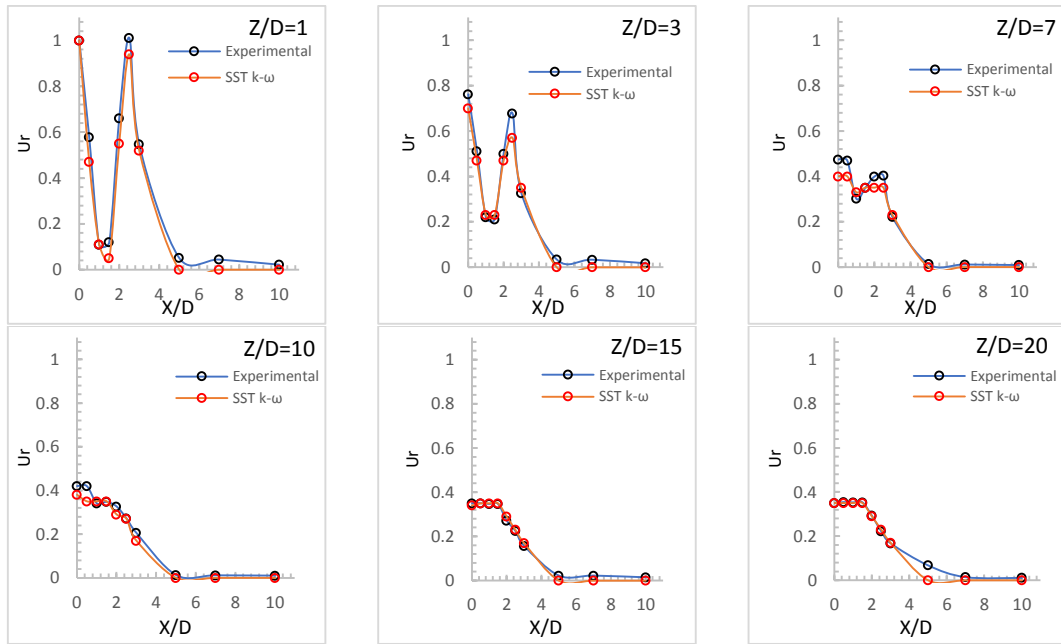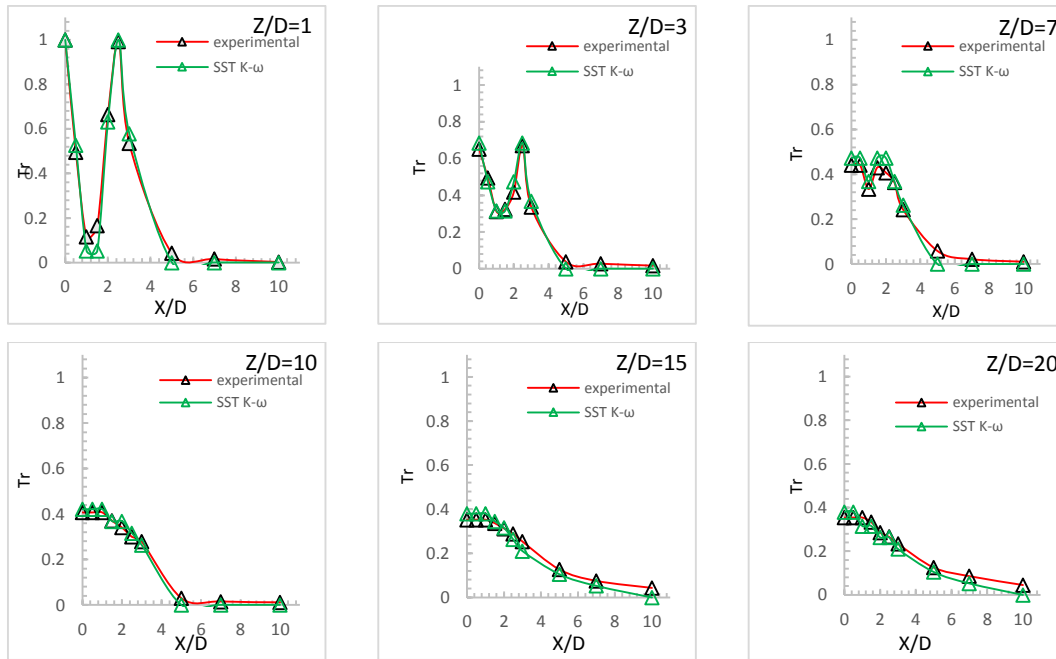
Fig. 15. Profiles of the velocity component U_r along X-direction at various axial locations (numerical and experimental results).
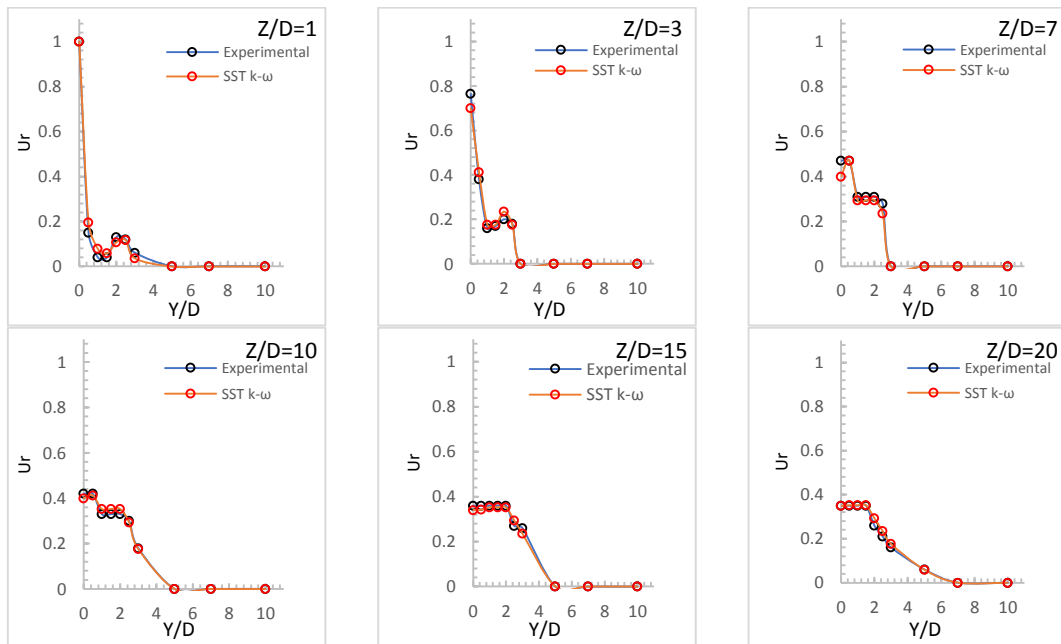

Fig. 16. Profiles of the velocity component U_r along Y-direction at various axial locations (numerical and experimental results).

This has been rigorously validated by experimental results which have been performed considering a configuration including a lobed central jet surrounded by six lobed peripheral jets. It has been found that this model properly predicts velocity and temperature's decay in the axial direction as well as their distributions along the X- and Y-directions over the entire studied domain. Thereby, it can be stated

that such a model can properly handle lobed jets interaction. Experimental and numerical analysis of the dynamic and thermal fields shows that the interaction between the jets leads to a redistribution of the velocity and the temperature in the mixed zone while allowing the spreading of the resulting jet. Three regions have been clearly identified: one (Z/D ≤ 1) that is close to the jets exit where they begin to

Fig. 17. Temperature profiles T_r along X-direction at various axial locations (numerical and experimental results).
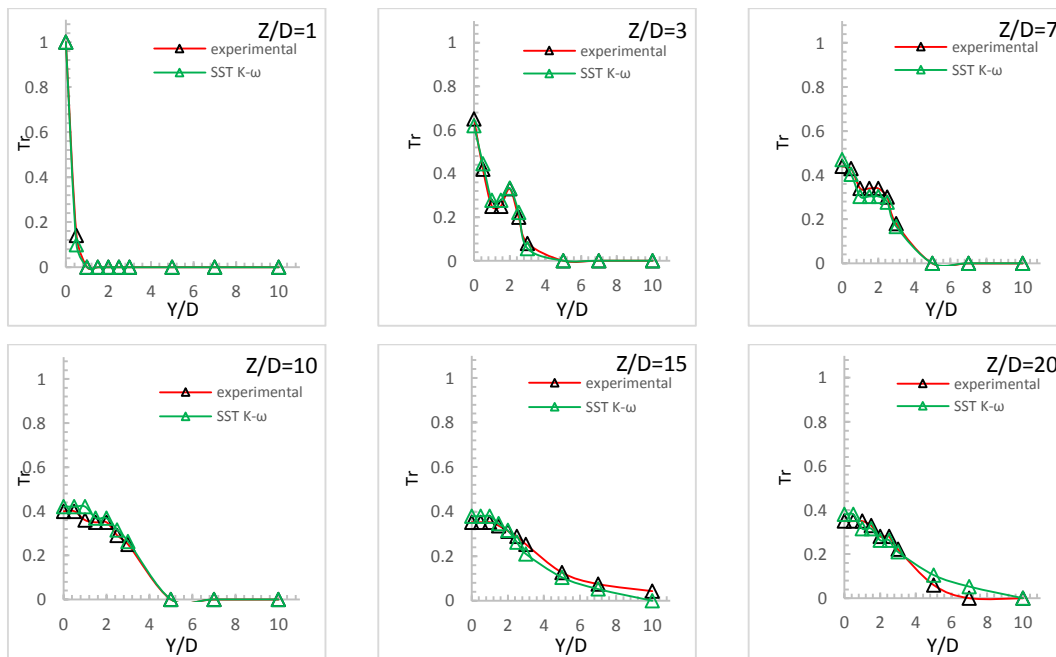

Fig. 18. Temperature profiles T_r along Y-direction at various axial locations (numerical and experimental results).

mix, a merging zone where jets interact fully while they mix, and a combination zone ($Z/D \geq 10$) very far from the exit with a single circular jet, result of complete mixing.

Based on the results obtained, it appears that the use of multiple lobed jets can be a promising solution to improve the ventilation systems performance of premises in terms of thermal comfort. This can help to come up with the best configuration that the manufacturer can integrate into air diffusion units via optimization studies of parameters such as the jets number, their location, and nozzles spacing.
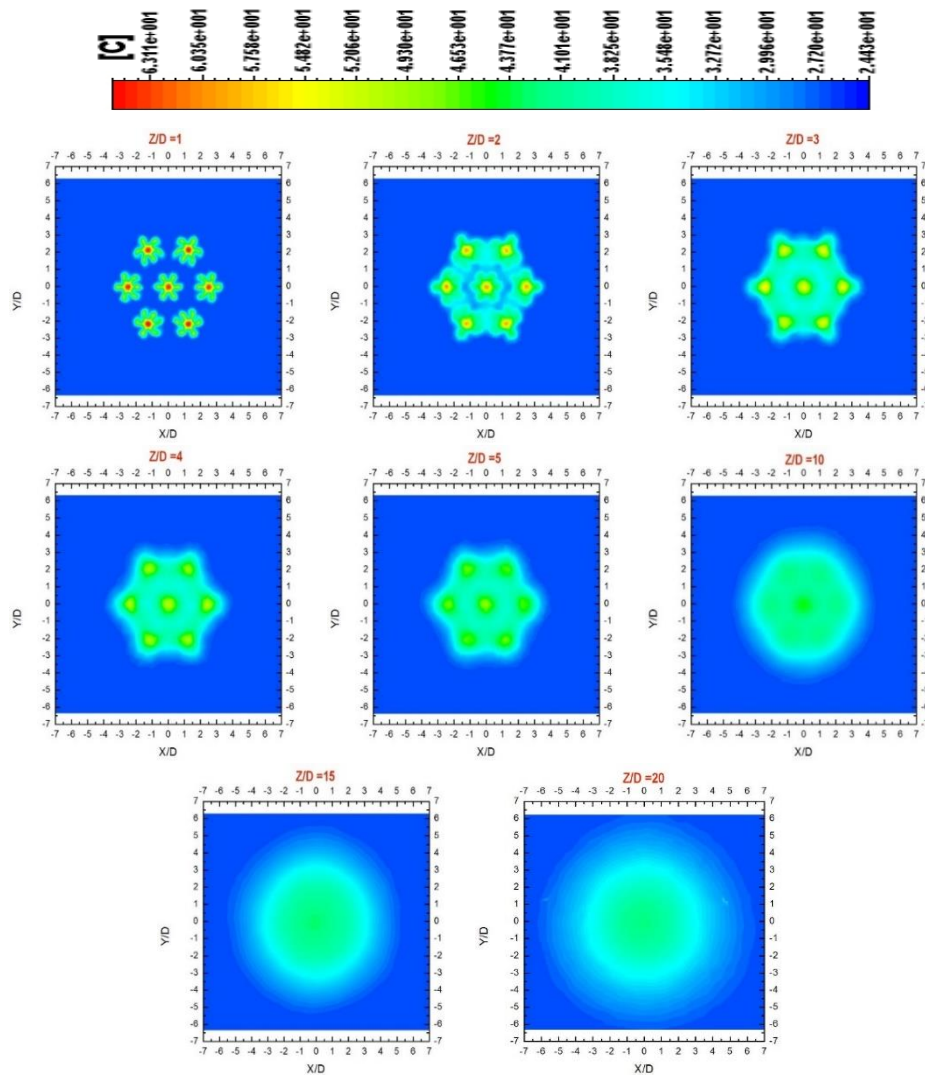
Fig. 19. Simulated average temperature contours with the SST k-ω model.

REFERENCES

Anderson, E. A. and R. E Spall (2001). Experimental and numerical investigation of two-dimensional parallel jets. *Transactions of the ASME* 123(2), 401-406.

Bennia, A., L. Loukarfi, A. Khelil, S. Mohamadi, M. Braikia and H. Naji (2016). Contribution to the experimental and numerical dynamic study of a turbulent jet issued from lobed diffuser. *Journal of Applied Fluid Mechanics*, 9(6), 2957-2967.

Bragança, P., K. Sodjavi and A. Meslem (2016). Thermal comfort in heating conditions with a ceiling mounted diffuser comparison of lobed and conventional diffusers. *CLIMA 2016 - Proceedings of the 12th REHVA World Congress*, Vol. 5, Heiselberg, P. K. (Ed.), Aalborg University, Denmark.

Braikia, M., L. Loukarfi, A. Khelil and H. Naji (2012). Improvement of thermal homogenization using multiple swirling jets.

Thermal Science 16(1), 239-250.

Chou, P. Y. (1945). On velocity correlations and the solutions of the equations of turbulent fluctuation. *Quarterly of applied mathematics* 3(1), 38-54.

Costa Rocha, P.A., H. H. B. Rocha, F. O. M. Carneiro, M. E. V. da Silva and C. F. de Andrade (2016). A case study on the calibration of the k- ω SST (shear stress transport) turbulence model for small scale wind turbines designed with cambered and symmetrical airfoils. *Energy 97*, 144-150.

Depuru Mohan, N. K., K. R. Prakash and N. R. Panchapakesan (2015). Mixing augmentation by multiple lobed jets. *American Journal of Fluid Dynamics* 5(2), 55-64.

Kannan, B.T. and N.R. Panchapakesan (2017). Influence of nozzle configuration on the flow field of multiple jets. *Journal of Aerospace Engineering* 232(9), 1639-1654.

Khelil, A., H. Naji, L. Loukarfi, M. HadjMeliani and

M. Braikia (2016). Numerical simulation of the interactions among multiple turbulent swirling jets mounted in unbalanced positions. *Applied Mathematical Modelling* 40(5-6), 3749-3763.

Lien, F. S. and M. A. Leschziner (1994). Assessment of turbulent transport models including non-linear RNG eddy-viscosity formulation and second-moment closure. *Computers & Fluids* 23(8), 983-1004.

Menter, F.R. (1994). Two-equation eddy-viscosity turbulence models for engineering applications, *AIAA Journal* 32(8), 1598-1605.

Menter, F.R. and Y. Egorov (2010). The scale-adaptive simulation method for unsteady turbulent flow predictions part 1: theory and model description. *Flow, Turbulence and Combustion* 85(1), 113-138.

Menter, F. R., M. M. Kuntz, and R. Langtry (2003). Ten years of industrial experience with the SST turbulence model. *Turbulence, Heat and Mass Transfer 4(1)*, 625-632.

Meslem, A., A. Dia, C. Beghein, M. El Hassan, I. Nastase and P. Vialle (2011). A comparison of three turbulence models for the prediction of parallel lobed jets in perforated panel optimization. *Building and Environment* 46(11), 2203-2219.

Meslem, A., I. Nastase and F. Allard (2010). Passive mixing control for innovative air diffusion terminal devices for buildings. *Building and Environment* 45(12), 2679-2688.

Meslem, A., I. Nastase and K. Abed-Meraim (2008). Experimental investigation of the mixing performance of a lobed jet flow. *Journal of Engineering Physics and Thermophysics* 81(1), 106.

Nastase, I. and A. Meslem (2008). Vortex dynamics and entrainment mechanisms in low Reynolds orifice jets. *Journal of visualization* 11(4), 309-318.

Nastase, I., A. Meslem, I. Vlad and I. Colda (2011). Lobed grilles for high mixing ventilation- an experimental analysis in a full-scale model room. *Building and Environment* 46(3),547-555.

Rotta, J. (1951). Statistische Theorie nichthomogener Turbulenz. *Zeitschrift für Physik* A 131(1), 51-77.

Versteeg, H. and W. Malalasekera (2007). *An introduction to computational fluid dynamics: the finite volume method*, 2nd Ed. Pearson, ISBN: 9780131274983.

Wilcox, C. D. (1998), *Turbulence modeling for CFD*. Third edition, ISBN-13: 978-1928729105.